Fatigue of short carbon fiber reinforced PEEK under compression: Influence of the load ratio and predictions from heat buildup measurements

Vanessa Kwiatkowski, Matthieu Le Saux, Vincent Le Saux, Sylvain Leclercq, Yann Marco

Pre-print of an article published in Fatigue & Fracture of Engineering Materials & Structures, 2023, 46, 2396-2410, doi: https://doi.org/10.1111/ffe.14003

Fatigue of short carbon fiber reinforced PEEK under compression: influence of the load ratio and predictions from heat build-up measurements

Vanessa Kwiatkowski[a,b]*, *Matthieu Le Saux*[a], *Vincent Le Saux*[a], *Sylvain Leclercq*[b], *Yann Marco*[a]

[a] *ENSTA Bretagne, UMR CNRS 6027, IRDL, F-29200 Brest, France*

[b] *Safran Landing Systems, 78140, Vélizy, France*

*vanessa.kwiatkowski@ensta-bretagne.org

Abstract: *Few works investigate the fatigue of short fiber reinforced thermoplastics under cyclic compression. Furthermore, the heat build-up approach to quickly predict the fatigue lifetime of these materials has not yet been investigated for compression-compression loadings. This paper first describes an experimental protocol to perform well-controlled cyclic compression tests without anti-buckling device that may induced bias. The uniaxiality of the global loading is checked during the test based on kinematic and thermoelastic coupling fields measurements. Then, the paper compares the results from fatigue and heat build-up tests performed on PolyEtherEtherKetone reinforced with 30 wt% of short carbon fibers, for several load ratios. It is shown that the fatigue lifetime is higher in compression than in tension and depends on the compression load ratio. The heat build-up approach appears to be relevant to quickly predict the fatigue lifetime of the material for the different loading ratios studied, including compression-compression.*

Keywords: Short fiber reinforced thermoplastics; Compression; Fatigue; Self-heating

1. Introduction

Interest in short carbon fiber reinforced thermoplastics is growing in the aerospace industry. The use of such materials allows the reduction of the weight of structures as well as an optimized cost. The injection molding process allows the high pace manufacturing of parts with stiffeners and ribs, for example, to overcome a lower rigidity

compared to metallic materials. Predicting the fatigue behavior of structures made of these materials raises many issues, notably due to the non-linear dissipative mechanical behavior of the matrix, and to the complex heterogeneous orientation distribution of the fibers, inducing a strong mechanical anisotropy.[1–3] In some industrial structures, the material can be subjected to fatigue under compression-compression cyclic loading. A lot of work has been done on short fiber reinforced thermoplastics (SFRT), in particular on polyamide reinforced with short glass fibers[2–6], but very little on fatigue under compressive loadings[7, 8].

For compression loadings, the main experimental difficulty is to guarantee the uniaxiality of the overall loading and avoid any buckling of the specimen. When the geometry of the material makes it possible, a cylindrical or cubical specimen can be directly set on compression plates.[9] This is not relevant for materials elaborated in the form of plates (with one dimension smaller than the two others). In this case, anti-buckling devices (standardized or not) are often used. For polymer matrix composite materials, different standard test methods for compressive properties are available, such as ASTM D6641[11] and ASTM D3410[12] that use an anti-buckling device. Non-standardized anti-buckling devices are also used sometimes.[5] Tabbed specimens with a reduce gauge length between the grips are used in some studies to reduce the risks of buckling under compression.[7,8] The first objective of this paper is to present a protocol to perform well-controlled cyclic compression tests and obtain reliable stress, strain and temperature data. In order to avoid any bias induced by anti-buckling devices (friction, inertia, rotation of the fixing elements…) and to be as non-intrusive as possible, the specimens are set directly in the hydraulic jaws. This configuration also enables future works changing the temperature and humidity conditions. The sample free length is optimized to avoid buckling of the sample while maintaining a sufficiently large gauge length so that the volume unaffected by the boundary conditions is large enough, and allows kinematic and temperature fields measurements. In addition, a particular attention is paid to the alignment of the jaws and the specimen during its installation. The loading conditions are checked during the tests on the basis of the analysis of kinematic and thermoelastic coupling fields (on the thickness-length planes of the sample).

Fatigue properties of SFRT have been studied in many works for the past few decades. The fatigue properties can depend on different parameters such as load ratio[2, 15, 16], sample

orientation[17, 18], temperature and humidity[3, 19]. This paper deals with PEEK reinforced with 30% in weight of short carbon fibers (PEEK CF30) and focuses on the effects of the load ratio. Indeed, PEEK is not sensitive to humidity[20] and not very sensitive to temperature in the range of interest (around 20°C), that is significantly below the glass transition temperature (about 150 °C)[21]. The effect of orientation, which is significant, is out of the scope of this paper. Most fatigue data in the literature are obtained for tension loadings or tension-compression loadings. For tension-compression loadings, it is observed that the mode of fatigue failure is driven by the tensile part of the loading.[3, 6] Few works investigate the fatigue of thermoplastics for compression-compression loadings and they focus on other materials than PEEK CF.[7, 22, 23] Another objective of this work is to characterize the fatigue lifetime of PEEK CF30 under compression-compression loading and compare it to that obtained in tension-tension loadings, and to analyze the influence of the load ratio. For that purpose, fatigue tests were performed for one specimen orientation (0° from the injection direction), three load ratios ($R = -\infty$, $R = 3$ and $R = 10$) in compression, one load ratio in tension-compression ($R = -1$) and one load ratio in tension ($R = 0$), at room temperature.

Fatigue campaigns are particularly time consuming for the type of material studied here, as the loading frequency cannot be too high to avoid excessive heat build-up which would induce biases. The ability of the heat build-up method to quickly evaluate the fatigue properties has been demonstrated for metallic materials[24, 25], elastomers[26] and more recently for some SFRT[4, 27]. The approach is to determine the dissipated energy per cycle from temperature measurements and then relate this energy to the fatigue lifetime. The heat build-up method with an empirical approach has been successfully applied by Leveuf *et al.*[4] to PEEK CF30 for cyclic tension ($R = 0$). The last objective of this paper is to study the ability of this approach to predict the fatigue lifetime of this material under compression loadings.

The first section of this paper presents the material and the experimental procedures used for heat build-up and fatigue tests. The protocol used to ensure the uniaxiality of the compressive loading, with a sample directly mounted in the hydraulic jaws, is then described. In the second section, the results of fatigue and heat build-up tests are presented. This section discussed the differences between compression-compression,

compression-tension and tension-tension test results as well as the effect of the load ratio. The third section provides an analysis of the approach to relate self-heating and fatigue lifetime.

2. Material and experimental procedures

2.1. Material and samples

The tested material is a PEEK thermoplastic reinforced with 30% in weight of short carbon fibers. The fiber diameter is 8 µm on average, with a standard deviation of 0.7 µm. The fiber length is 130 µm on average, with a standard deviation of 80 µm. The samples are milled from 5 mm-thick, 150 mm x 250 mm, injection molded plates, as shown in Fig 1. The typical distribution of the orientation of the fibers through the plate thickness is represented in Fig 2 by the components a_{11}, a_{22} and a_{33} of the second-order fiber orientation tensor, expressed in the orthonormal basis $(\overrightarrow{e_1}, \overrightarrow{e_2}, \overrightarrow{e_3})$, where $\overrightarrow{e_1}$ and $\overrightarrow{e_3}$ are along the injection direction and the plate thickness, respectively. These orientation tensors are obtained by the analysis of images obtained using X-ray microtomography.

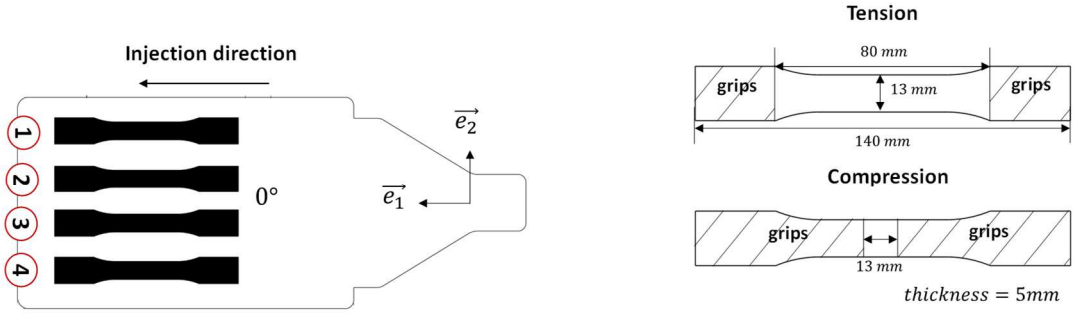

Fig 1. Samples taken from the plate, dimensions of the samples for tension and compression tests.

They are shown in Fig 2 for four samples taken at different positions in two plates. The microstructure is homogeneous in the same plate and identical from one plate to another. It is possible to distinguish the skin-core microstructure, *i.e.*, the fibers are mainly oriented along the injection direction in the skins, and perpendicular to this direction in the core. The fiber orientation distribution along the plate thickness is symmetric. The samples cut from the plates have a dogbone shape so that they can be used for both compression and tension tests. They are cut with their gauge main axis at 0° from the injection direction. As shown in Fig 2, the sample gauge has a width of 13 mm and a length of 80 mm for

tensile tests and 13 mm for compression tests. The length of 13 mm used for compression tests was chosen because it avoids buckling in compression while ensuring a homogeneous deformation zone and allowing kinematic and temperature field measurements.

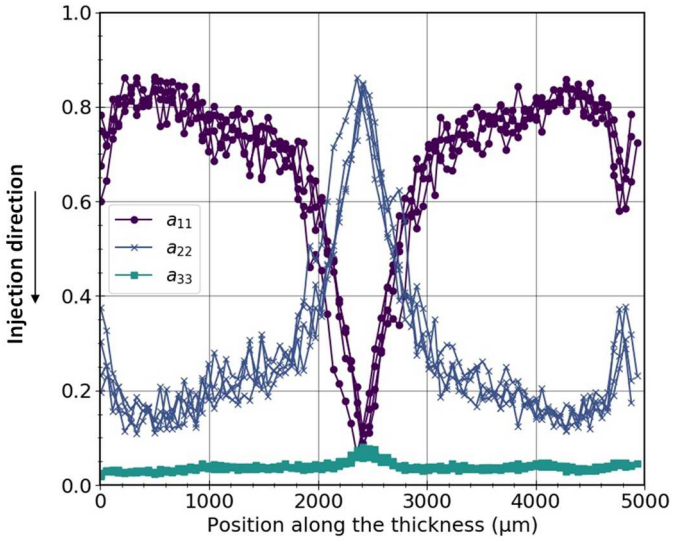

Fig 2. Distribution of the diagonal components of the fiber orientation tensor along the thickness of four samples taken at different positions in two plates.

2.2. Experimental procedures

The tests have been performed on a MTS servo-hydraulic testing machine with a capacity of 50 kN. They were performed at room temperature (around 25°C, not controlled) and humidity. It was measured that the temperature rise of the samples during the tests did not exceed 10°C. The sample temperature was therefore always much lower than the glass transition temperature. Thus, the temperature variations are not supposed to have any effect on the results. A load-controlled sinusoidal loading was applied with a frequency of $2\,Hz$ for heat build-up tests or $4\,Hz$ for heat build-up and fatigue tests. A special attention was paid to the set-up to verify the correct alignment of the jaws and the samples with respect to the loading direction. This point is discussed in section 2.4. The load ratios studied are $R = -\infty$, $R = 10$ and $R = 3$ (compression-compression), $R = -1$ (tension-compression) and $R = 0$ (tension-tension).

The nominal stress is calculated from the ratio of the force measured to the initial cross-section of the sample gauge. Fig 3 shows examples of stress evolutions for different load ratios with the same maximum stress in absolute value. For confidentiality reasons, stress

levels are normalized in the paper, by a single value so that the effects of the load ratio can be analyzed.

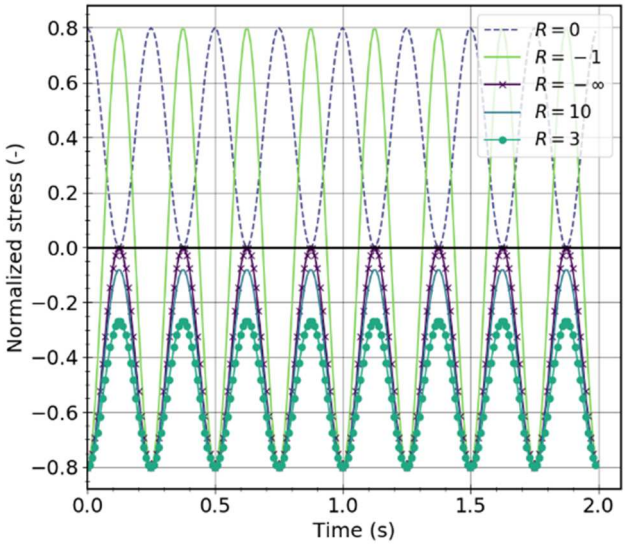

Fig 3. Examples of stress curves for a loading frequency of 4 Hz for the different load ratios tested.

Fig 4 shows the experimental setup used. The kinematic fields were measured on one side (thickness-length plane) of the sample by digital image stereo-correlation. To do so, a random speckle pattern was sprayed on the sample surface using black and white paint, as shown in Fig 5. The material, the acquisition parameters and the analysis parameters used for digital image stereo-correlation are given in Table 1.

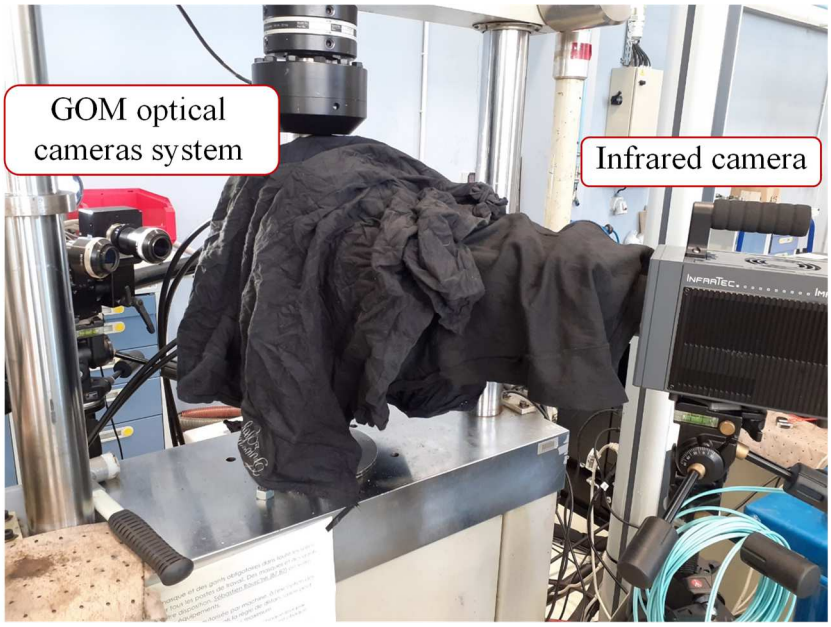

Fig 4. Experimental setup: optical cameras system on the left side and infrared camera on the right side.

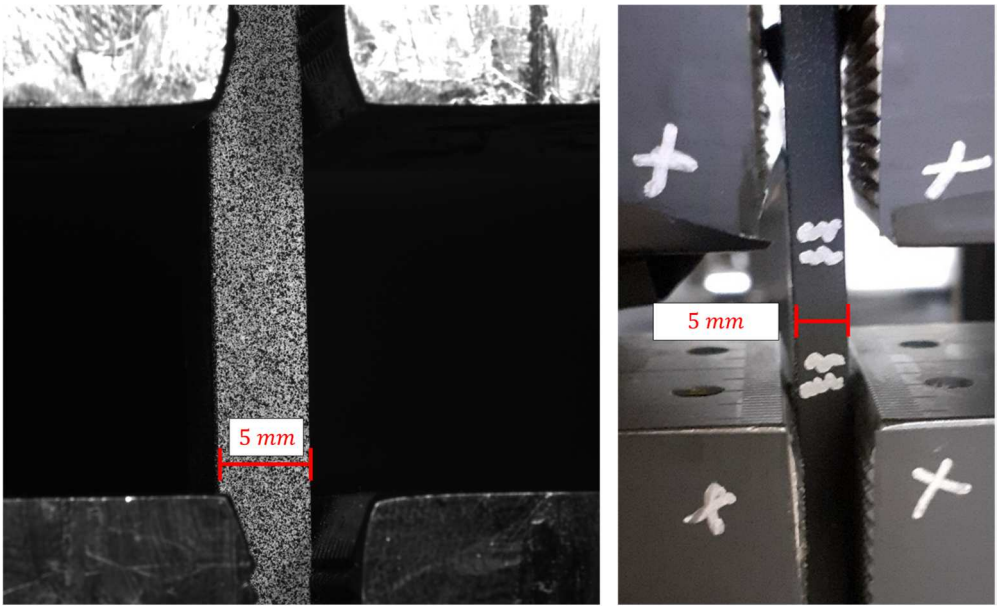

Fig 5. Side of a sample sprayed with a random speckle pattern with black and white paint for image stereo-correlation (left figure), positioning of the specimen (side painted in black for infrared measurements and with low emissivity markers for motion compensation) in the hydraulic jaws for compression tests (right figure).

Table 1 Material, acquisition parameters and analysis parameters used for digital image correlation (n.a.: not available).

Material and acquisition parameters	
Camera	GOM 4M
Image resolution	2352 x 1728 pixels
Lens	75 mm lens (ARAMIS 4M)
Aperture	n.a.
Field-of-view	25 mm x 18 mm
Image scale	30 µm/pixel
Stereo-angle	25°
Stand-off distance	50 mm
Image acquisition rate	60 Hz
Exposure time	14 ms
Pattern feature size	10-15 pixels
Analysis parameters	
DIC software	Aramis v 6.3
Image filtering	No filtering
Subset size	21 x 21 pixels
Step size	11 pixels
Subset shape function	Linear
Matching criterion	n.a.
Interpolant	n.a.
Strain window	3 pixels x 3 pixels
Virtual strain gauge size	43 pixels
Strain formulation	Green-Lagrange
Post-filtering of strains	No post-filtering
Displacement noise-floor	0.3-0.5 µm
Strain noise-floor	5.10^4

The temperature field was measured on the other side of the sample (and then to determine the fields of thermoelastic coupling and dissipated energy) using an infrared camera. This sample surface was painted with a high emissivity black paint to limit the influence of the environment on measurements as much as possible. High emissivity markers were also applied to the sample surface to perform motion compensation from infrared image correlation, as shown in Fig 5. A black box and a dark fabric surrounded the sample and the grips, as illustrated in Fig 4. The material and the parameters used for infrared measurements are given in Table 2. The camera was fixed and the sample was moving during the experiments. Consequently, each pixel of the image does not always correspond to the same area of the sample. To get a consistent estimate of the temperature evolution, a motion compensation was applied. It is based on the analysis of the displacements of low-emissivity markers applied on the sample (Fig 5), using the method presented in the in-house software Celenos[30] and used by Navrátil *et al.*[29].

Table 2 Camera and parameters used for temperature measurements.

Camera	InfraTec ImageIR 10300
Image resolution	1920 x 1536 pixels
Field-of-view	25 mm x 18 mm
Image scale	75 µm/pixel
Image acquisition rate	100 Hz
Calibration	Built-in
Noise equivalent temperature difference	30 mK

The fatigue tests were performed at a loading frequency of 4 Hz. The investigated range of stress leads to failure between 10^3 cycles and more than 10^6 cycles.

2.3. Heat build-up tests

The basic idea of heat build-up tests is to apply a succession of steps of cyclic loadings with increasing stress amplitude to a sample and to record the evolution of the temperature for each sequence. These measurements are then used to determine the cyclic (*i.e.*, per cycle) dissipated energy Δ^* and the amplitude of the thermo-elastic coupling C_e. Δ^* can potentially be related to the fatigue lifetime, as discussed in section 4. C_e is related to the

stress state (and the thermal expansion). As discussed in the next section, the field of C_e is used (in addition to the kinematic fields) to verify that the global loading is uniaxial.

In this study, an adiabatic approach is used to analyze the temperature measurements. The protocol thus focuses on the first loading cycles, which limits any potential damage accumulation during the experiment. Each loading block is composed of two stages. The first stage is the loading step: the sample is subjected to 30 cycles with given minimum and maximum stresses. The second stage is a cooling step during which the sample (held at the minimum stress level in absolute value) cools down to the ambient temperature. The last loading block is run until failure of the sample. The determination of the cyclic (*i.e.*, per cycle) dissipated energy Δ^* and the thermo-elastic coupling C_e relies on the resolution of the heat equation.[28] Under some assumptions, including adiabaticity, the heat equation can be written as:[4, 29]

$$\rho C_p \frac{\partial \theta}{\partial t}_{t\to 0} = f\Delta^* + C_e \quad (1)$$

with ρ the material density, C_p the specific heat, θ the temperature variation and f the mechanical loading frequency. The solution of the equation (1) for a sinusoidal cyclic loading can be written as follows.[4]

$$\theta(t) = \dot{\theta}_0 t + C_e \sin(2\pi f t + \phi) \quad (2)$$

with $\dot{\theta}_0 = \frac{f}{\rho C_p}\Delta^*$.

The spatial average of the cyclic dissipated energy is determined from the mean temperature (0D approach) over the thickness-length surface of the sample. Fig 6 shows an example of temperature map obtained. The vertical temperature gradient observed is due to the heat coming from the lower hydraulic grip. Before starting the test, the specimen is held in the jaws until the temperature gradient no longer changes. It is assumed that the gradient does not change during the test. Furthermore, it is the specimen temperature evolution with respect to the temperature field obtained at the beginning of the test that is analyzed. The temperature gradient therefore does not interfere with the analysis. Fig 6 presents the typical evolution of the mean temperature variation measured during one block of 30 cycles. The temperature variation θ is calculated from the difference between the temperature of the tested sample and the temperature of a

reference sample of the same material, also painted in black and placed in the observation area. The identification of Δ^* is related to the mean temperature increase rate $\dot{\theta}_0$ from equation (2). It is performed on a specific time window according to four hypotheses. The first one is that the thermo-elastic coupling compensates over a cycle. The second one is that the cyclic dissipated energy is constant from one cycle to another. The third one is the adiabatic condition; the time window considered to perform the analysis has to be significantly shorter than the characteristic time for thermal exchanges. The characteristic time, evaluated from the temperature drop during the cooling step, is around $40s$ in the present case. The last requirement is that the machine regulates the mechanical loading properly. Consequently, the identification of $\dot{\theta}_0$ is was performed after the 4th cycle, from which the applied force follows the input command, and over a temporal window of 5s which is well below the characteristic time, as illustrated in Fig 6. The function identified fits the experimental signal very well and the linearity of the evolution of the mean temperature per cycle supports that the adiabaticity conditions are met (Fig 6).

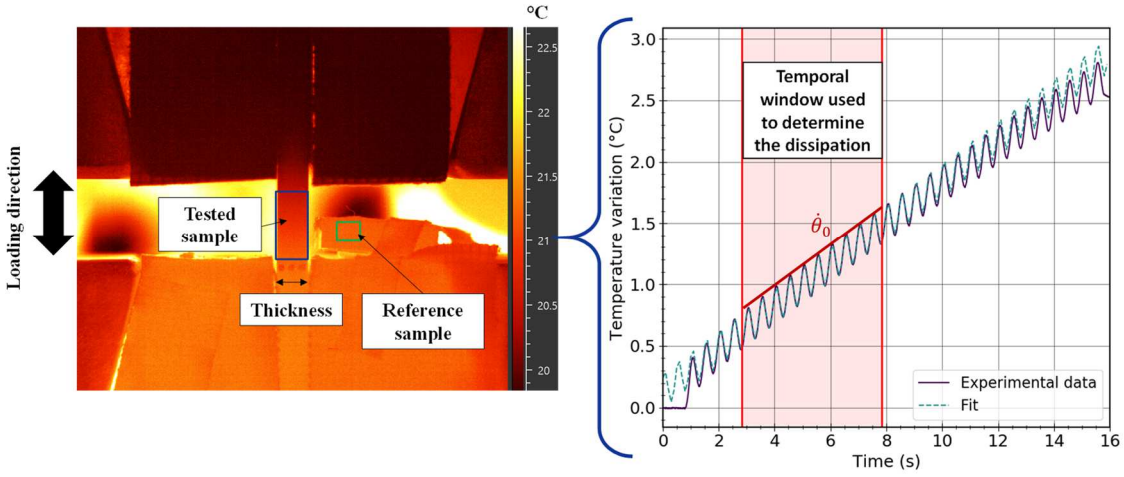

Fig 6. Temperature field (left) and temporal evolution of the mean temperature variation θ in the region of interest (right) for a cyclic compression test performed with a frequency of 2 Hz.

The amplitude of the thermo-elastic coupling is obtained at each pixel in the region of interest from a pixelwise analysis of the temperature evolution (Eq 2) using the lock-in method introduced by Breitenstein *et al.*[31]

2.4. Verification of the compressive loading

A special attention was paid to the correct alignment of the jaws and the specimen during its installation, according to the loading direction. This simple attention is not always enough. For example, on a machine too compliant, with no locking in rotation of the cylinders, or grips not rigid enough, a misalignment of the jaws has been observed during some tests, even though the initial proper alignment was checked. This misalignment causes heterogeneous loading with bending and shear in addition to compression ("buckling" of the specimen). Therefore, an experimental procedure has been developed to detect a potential misalignment of the jaws and verify that the loading remains uniaxial also during the test. The procedure consists in verifying the symmetry of the kinematic field and the thermo-elastic coupling field along the thickness of the sample side surface. These fields are determined from image stereo-correlation and infrared measurements, respectively. Indeed, as the microstructure of the material is symmetrical according to the sample thickness, the kinematic and thermo-elastic coupling fields are also supposed to be symmetrical if the loading is uniaxial.

Fig 7 and Fig 8 show the transverse strain and longitudinal strain fields as well as the thermo-elastic coupling field, determined on specimens for which the global loading is considered as non-uniaxial and uniaxial, respectively. If the global loading is uniaxial, the longitudinal strain is expected to be homogeneous within the sample because the displacement imposed during the test at the sample extremities is homogeneous. Due to the gradient of microstructure along the sample thickness, a gradient of transverse strain (related to the effective Poisson ratio in particular) and of C_e (related to stress) is expected along this direction because the material mechanical behavior is anisotropic and depends on the microstructure. When the global loading is uniaxial, the gradient of transverse strain and C_e are expected to be symmetric along the sample thickness with respect to mid-thickness. For each field, profiles are plotted along the sample thickness for two areas of the region of the interest. They are obtained by calculating the mean value over 4 pixels along the longitudinal direction, represented by the rectangles in Fig 7 and Fig 8. The profiles are normalized by the average of the quantities measured in the two skins areas (corresponding to 1 mm on each side of the thickness).

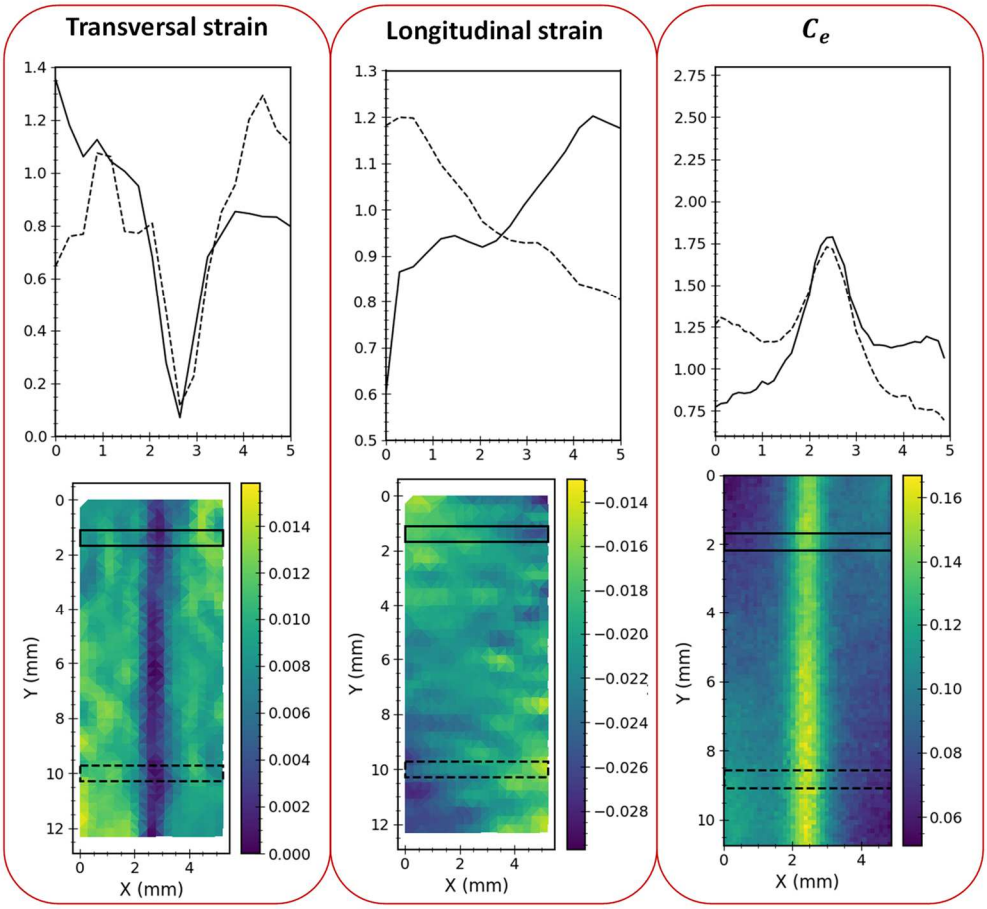

Fig 7. Case of a compression test considered as non-uniaxial: transverse strain field (left), longitudinal strain field (middle), and thermo-elastic coupling field (right), with the associated normalized profiles along the thickness for a normalized maximum stress level in absolute value of 0.86 (X and Y correspond to the sample thickness and length, respectively; the loading is applied along Y).

For the case considered as non-uniaxial (Fig 7), the thermo-elastic coupling and the strain fields are asymmetrical according to the skins and heterogeneous along the sample length. The relative difference between the two skins is about 40-50%. This is due to the connection of the grips to the machine and to a slight displacement and rotation during the tests, which induced a misalignment of the grips.

For the case considered as uniaxial (Fig 8), the thermo-elastic coupling and the strain fields are almost symmetrical with respect to the mid-thickness and uniform along the longitudinal direction. The relative difference between the two skins is lower than 10%. These results show the capability to detect a misalignment of the jaws during a test thanks

to the analysis of the thermo-elastic coupling or strain fields. For all the tests presented below, systematic monitoring checked that the relative difference in thermoelastic coupling and strain between the two skins of the sample at a given axial position is below 10%.

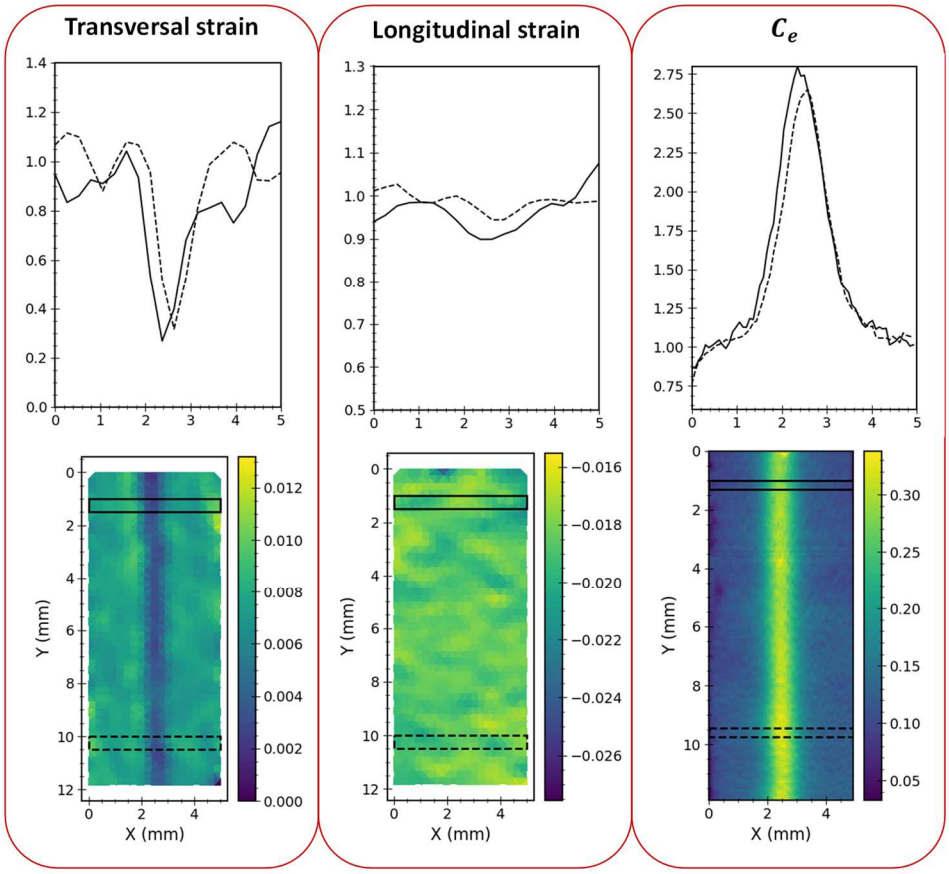

Fig 8. Case of a compression test considered as uniaxial: transverse strain field (left), longitudinal strain field (middle), and thermo-elastic coupling field (right), with the associated normalized profiles along the thickness for a normalized maximum stress level in absolute value of 0.83 (X and Y corresponds to the sample thickness and length, respectively; the loading is applied along Y).

3. Results

3.1. Fatigue

The majority of the tests were conducted until the sample broke. The number of cycles to failure reported corresponds to the total failure of the sample. Failure in compression occurred in the sample gauge length, according to a plane inclined of approximately 45°

with respect to the global compression direction, as shown in Fig 9. This suggests that macroscale failure is dominated by shear. Further discussion on the failure mechanisms at the microscale requires detailed microscopic analysis and is out of the scope of this paper.

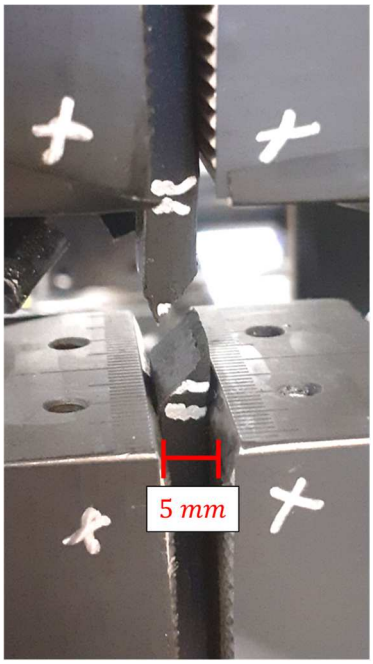

Fig 9. Failure in compression of a sample.

Fig 10 (left figure) shows the results of the fatigue tests performed on 0° samples at $R = 10$, $R = 3$, $R = -\infty$, $R = -1$ and $R = 0$, as a function of the maximum stress in absolute value. An arrow to the right indicates the tests interrupted before failure (no break). For a given maximum stress in absolute value, it can be observed:

- a fatigue lifetime higher in compression ($R = -\infty$) than in tension ($R = 0$) with a factor of more than two decades;
- a fatigue lifetime shorter for $R = -\infty$ than for $R = 10$ and $R = 3$ (*i.e.*, when the stress amplitude is higher);
- a fatigue lifetime shorter for $R = -1$ than for the other load ratios studied.

Fig 10 (right figure) presents the fatigue results as a function of the stress amplitude. For a given stress amplitude:

- the number of cycles to failure is higher in compression than in tension;

- the fatigue lifetime in compression is significantly lower (about three decades) for $R = 3$ than for $R = 10$ or $R = -\infty$ (*i.e.*, when the mean or maximum stress in absolute value is higher);
- the fatigue lifetime for $R = -1$ is longer than for $R = 0$ and shorter than for $R = -\infty$.

In conclusion, the results show a better fatigue resistance of the material in compression than in tension at equivalent loading conditions, and a significant influence of the load ratio.

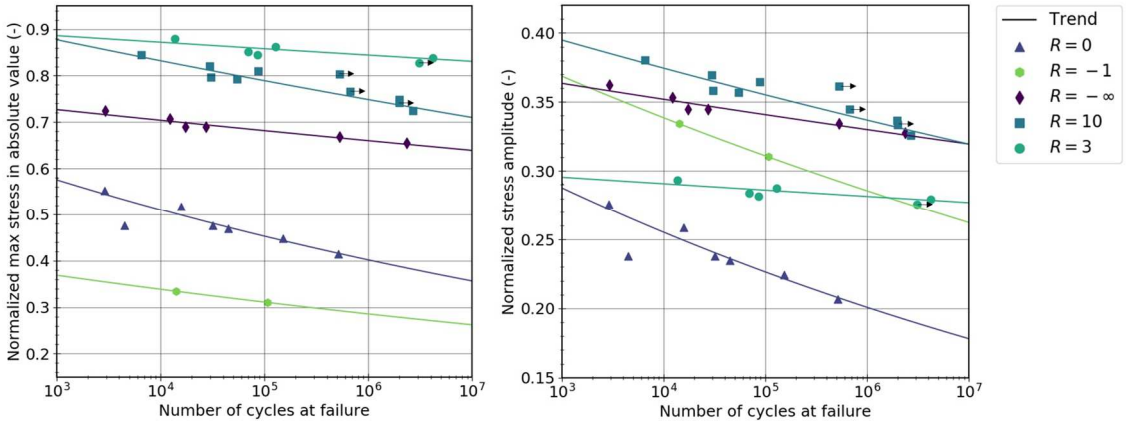

Fig 10. Fatigue test results according to the maximum stress amplitude (left figure) and according to the stress amplitude (right figure) for $R = 0$, $R = -\infty$, $R = 10$, $R = -1$ and $R = 3$ (loading frequency of 4 Hz) and associated trends (using a Basquin power law) (arrows to the right indicate that the test was interrupted before the sample broke).

3.2. Heat build-up

The first step to apply the heat build-up method in fatigue life prediction is to verify different hypotheses, which are:

- the repeatability of the tests,
- the independence of the cyclic dissipated energy to the loading history, and the consistency between the results from heat build-up and fatigue tests (*i.e.*, without previous loading blocks at lower stress levels),
- the independence of the cyclic dissipated energy to the load frequency.

Fig 11 shows heat build-up curves for 0° sample at $R = 10$ for different loading histories and different load frequencies ($2\ Hz$ and $4\ Hz$). According to the results, the tests are repeatable and there is no dependency to the loading frequency and to the loading history. The hypotheses are validated for all load ratios.

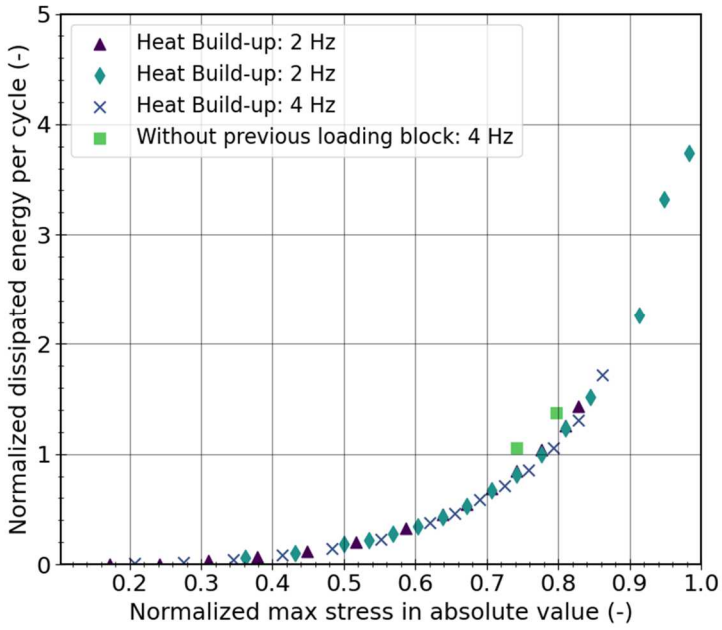

Fig 11. Heat build-up curves for R=10, for different loading histories and frequencies of 2 Hz and 4 Hz; comparison to the cyclic dissipated energy obtained without previous loading at lower stress levels.

The heat build-up curves obtained at $R = 10$, $R = 3$, $R = 0$, $R = -1$ and $R = -\infty$ for a load frequency of $4\ Hz$ are shown in Fig 12 according to the maximal stress in absolute value and in Fig 13 according to the stress amplitude. First, for the same value of maximum stress in absolute value (Fig 12), one can notice:

- similar dissipated energy in tension ($R = 0$) and in compression ($R = -\infty$);
- a decrease of the dissipated energy when the load ratio evolves from $R = -\infty$ to $R = 10$ then to $R = 3$; this decrease is related to a decrease of the stress amplitude (Fig 3);
- a higher dissipated energy for $R = -1$ than for the other load ratios studied.

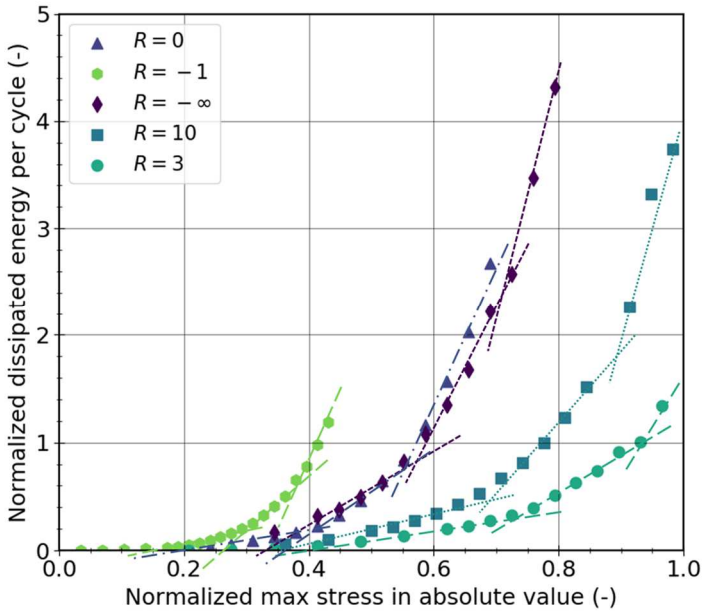

Fig 12. Heat build-up curves as a function of the maximal stress in absolute value for $R = 0$,$R = -1$, $R = -\infty$, $R = 10$ *and* $R = 3$, *for a loading frequency of 4 Hz; the lines correspond to the three dissipation regimes identified to make the link between fatigue and heat build-up.*

According to Fig 13, the dissipated energy per cycle is similar in compression ($R = -\infty$) and in tension ($R = 0$) for a given stress amplitude (at least up to a normalized stress amplitude of about 0.3). For a same stress amplitude, the cyclic dissipation does not evolve monotonically with the load ratio (for $R = 3$, it is higher than for $R = 10$ and lower than for $R = -\infty$). The cyclic dissipation is shorter for $R = -1$ than the other load ratios studied.

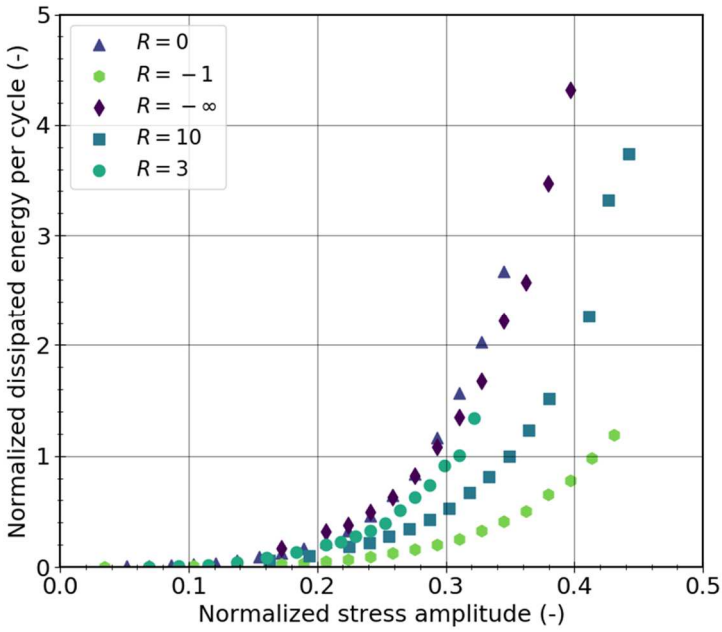

Fig 13. Heat build-up curves as a function of the stress amplitude for $R = 0$*,* $R = -\infty$*,* $R = 10$*,* $R = -1$ *and* $R = 3$*, for a loading frequency of 4 Hz.*

4. Link between fatigue and heat build-up

The heat build-up curve provides a relation between the stress and the dissipated energy. The objective is to relate the dissipated energy and the fatigue lifetime through an energy-based criterion. Fig 14 shows the dissipated energy per cycle as a function of the number of cycles at failure obtained from fatigue tests for $R = 0$, $R = -\infty$, $R = 10$, $R = -1$ and $R = 3$. For the same number of cycles at failure, the dissipated energy per cycle:

- is higher for compressive loading ($R = -\infty$) than for tensile loading ($R = 0$), while it is similar for the same maximum or alternate stress, as discussed above;
- is close for $R = -\infty$ and $R = 10$, and lower for $R = 3$.

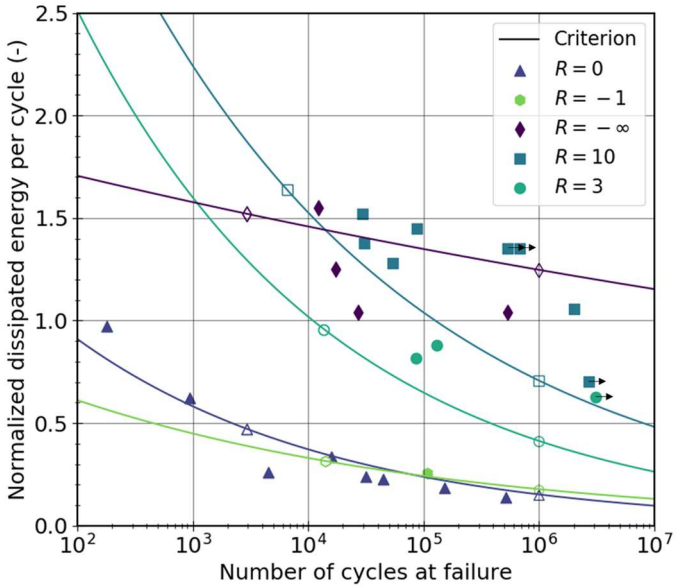

Fig 14. Dissipated energy per cycle as a function of the number of cycles at failure for $R = 0$, $R = -\infty$, $R = 10$, $R = -1$ *and* $R = 3$*: comparison of experimental results (the arrows to the right indicate that the test was interrupted before the sample broke) and predictions by the fatigue criterion in equation (3) (one set of parameters for each load ratio).*

To relate the energy dissipated per cycle to the number of cycles to failure from the heat-build up test results, the approach presented by Leveuf *et al.*[4] is followed. It consists in an empirical analysis based on a threshold criterion. This criterion relates the number of cycles to failure N_f to the cyclic dissipated energy Δ^* as follows:

$$\Delta^* N_f^b = C \tag{3}$$

with b and C two parameters to identify.

Consequently, two sets (Δ^*, N_f) are needed to identify b and C parameters from the equation (3). The first set (Δ_R^*, N_R) corresponds to a fatigue test during which the temperature measured on the region of interest has stabilized. The second set $(\Delta_{10^6}, N_{10^6})$ is determined from the analysis of the heat build-up curve.

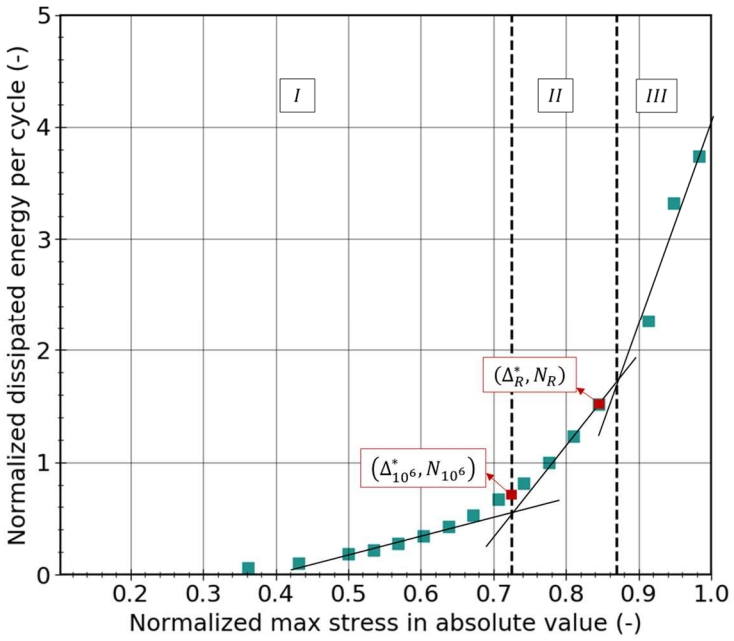

Fig 15. Heat build-up curves for $R = 10$ and a loading frequency of 4 Hz, with three regimes and two sets (Δ^*, N_f) identified.

To do so, three regimes are identified on the heat build-up curves based on a graphical analysis, as shown in Fig 15. First the third regime is identified over the last points, then the second regime from the change of slope and finally the first one. The set $(\Delta_{10^6}, N_{10^6})$ corresponds to the transition between the first regime and the second regime in the heat build-up curve. As done by Leveuf *et al.*[4], it is assumed that the dissipated energy determined at this transition corresponds to a fatigue life of 10^6 cycles, which is an arbitrary value. Here, only 30 cycles are performed for each loading block since the evaluation of the cyclic dissipated energy is performed on a few cycles. This limits potential damage accumulation during the heat build-up test. It is assumed that the three regimes correspond to the appearance of different dissipative mechanisms such as viscoelasticity, plasticity or damage.[1, 32] The identification of the regimes for all the conditions tested is presented in Fig 12.

One set of parameters b and C is identified for each experimental condition from the two sets (Δ^*, N_f). Fig 14 compares the dissipated energies per cycle as a function of the number of cycles at failure obtained from fatigue tests to those predicted by the fatigue criterion (equation (3)) once adjusted from the analysis of the heat-build up data. The

predictions are relatively close to the experimental results for $R = -1$, $R = 0$ and $R = -\infty$. The predictions tend to underestimate a little the cyclic dissipated energy for a given number of cycles at failure for $R = 10$ and $R = 3$.

Then, to be able to relate the number of cycles to failure to the maximum stress, the relation between the dissipated energy and the maximum stress in absolute value (*i.e.*, the heat build-up curve) is fitted by a fourth-order polynomial function, as shown in Fig 16. This is done for the four load ratios tested.

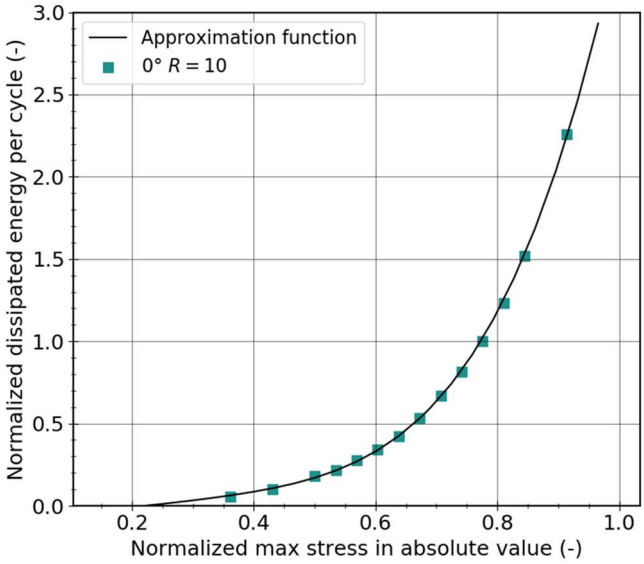

Fig 16. Approximation of the heat build-up curves by a fourth-order polynomial function for 0° sample, $R = 10$ *and a loading frequency of* 4 Hz.

Finally, the number of cycles to failure can be predicted from the maximum applied stress. Fig 17 compares the number of cycles to failure predicted using this method and the experimental ones, as a function of the maximum stress applied, for the different load ratios studied. The predictions are satisfactory for the different load ratios. They are better for $R = 0$ and $R = -1$ (failure controlled tension. For $R = -\infty$, R=10 and $R = 3$, *i.e.*, for compression-compression loadings, beyond 10^6 cycles, the predictions tend to significantly underestimate the number of cycles at failure for a given maximum stress. Recall that the parameters in the criterion are identified using only two points. The predictions from the criterion are therefore very sensitive to the points chosen. The first point is obtained from one single fatigue test and does not necessarily correspond to the average of the statistical distribution of the data. The second point is determined from the

empirical analysis of the heat build-up curve to identify the transition corresponds to a fatigue life of 10^6 cycles, as done by Leveuf *et al.*[4] for tension loading. The predictions obtained by considering that the transition between the two first dissipation regimes corresponds to a fatigue life of 10^7 are shown in Fig 18. The predictions are slightly worse for $R = 0$ and $R = -1$ but are improved for compression-compression loading, *i.e.*, for $R = -\infty$, $R = 10$ and $R = 3$ ratios. The prediction beyond 10^6 cycles could be improved by defining a threshold beyond which the fatigue criterion changes or by enriching the energy-based criterion. To refine the analysis of the heat build-up results and to support the link between heat build-up and fatigue life, it would be necessary (i) to develop a mechanical behavior law able to predict the contributions of the different dissipative phenomena to the total dissipation, as done in by Leveuf *et al.*[1] and Navrátil *et al.*[32], and/or (ii) to analyze the damage mechanisms, as done by Marco *et al.*[26] for rubber materials for example.

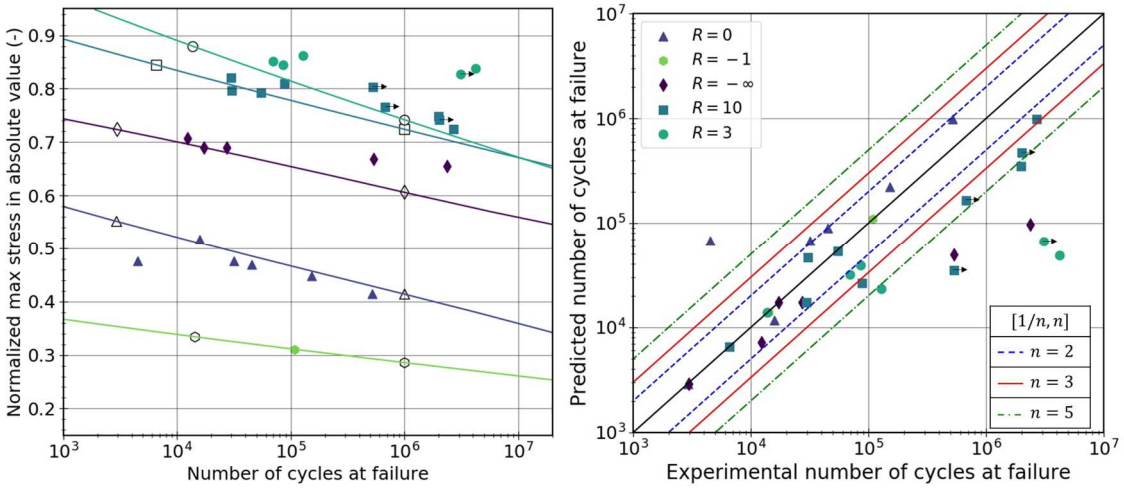

Fig 17. Fatigue test results (symbols) for R=0, R=-∞, R=10, R=-1 and R=3 with a loading frequency of 4 Hz; comparison to predictions (lines) by the dissipated energy-based criterion determined from heat build-up results considering that the transition between the two first dissipation regimes corresponds to a fatigue life of 10^6 cycles (the empty symbols correspond to the points associated with (Δ_R^*, N_R) and $(\Delta_{10^6}, N_{10^6})$) (left figure); comparison between predicted and experimental numbers of cycles at failure (right figure).

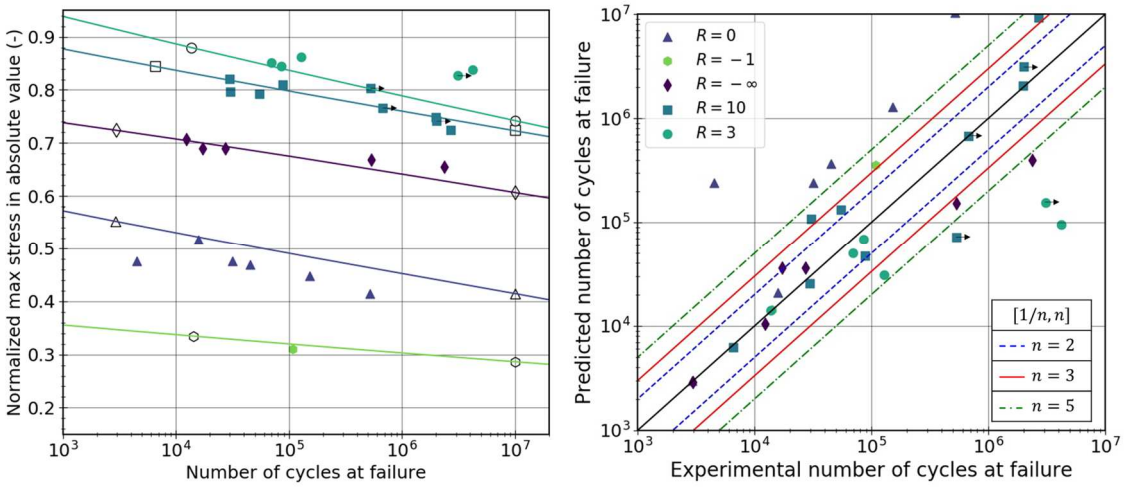

Fig 18. Fatigue test results (symbols) for R=0, R=-∞, R=10, R=-1 and R=3 with a loading frequency of 4 Hz; comparison to predictions (lines) by the dissipated energy-based criterion determined from heat build-up results considering that the transition between the two first dissipation regimes corresponds to a fatigue life of 10^7 cycles (the empty symbols correspond to the points associated with (Δ_R^*, N_R) and $(\Delta_{10^7}, N_{10^7})$) (left figure); comparison between predicted and experimental numbers of cycles at failure (right figure).

The fatigue criterion investigated in this paper, based on the dissipated energy, is not able to predict the fatigue lifetime for the different load ratios in a unified manner (*e.g.*, with one set of parameters). The stress-strain data measured during the fatigue tests could be used to calculate quantities (*e.g.*, elastic energy, hysteresis energy, cyclic creep energy, etc.) to establish a failure criterion capable of predicting fatigue lifetime in a unified manner, for load ratios as well as for different orientations, as done by Santharam *et al.*[3].

5. Conclusion and perspectives

This paper deals with the fatigue behavior of PEEK CF30 for compressive loadings. The first objective was to propose an experimental procedure to perform well-controlled cyclic compression tests without anti-buckling device, allowing to obtain reliable stress, strain and temperature data. The samples are mounted directly in the hydraulic jaws of the machine to avoid any bias that could result from the use of an anti-buckling device. The free length of the sample is optimized to avoid any buckling while ensuring a homogeneous deformation zone and allowing kinematic and temperature fields measurements. A special attention is paid to the correct alignment of the jaws and the specimen during its installation. The uniaxiality of the loading during the test is verified

from kinematic fields determined by images stereo-correlation and thermo-elastic coupling fields obtained from infrared measurements.

The second objective was to characterize the fatigue lifetime of PEEK CF30 under compression-compression loadings ($R = -\infty$, $R = 10$ and $R = 3$), tension-compression loadings ($R = -1$) and tension-tension loadings ($R = 0$), for one sample orientation (0° from the injection direction), at room temperature (and humidity), and to analyze the influence of the load ratio. The results of the fatigue tests show that fatigue lifetime is higher in compression than in tension and depends on the compression load ratio. The heat build-up curves show that the cyclic dissipated energy is similar in tension and in compression and dependent on the load ratio.

The third objective was to apply the empirical approach validated by Leveuf *et al.*[4] for tension loading to the results obtained in compression, to quickly predict the fatigue lifetime from heat build-up measurement, using a fatigue criterion based on the cyclic dissipated energy. The approach seems relevant but gives too conservative predictions for large numbers of cycles (beyond 10^6 cycles typically). For larger fatigue lifetimes, the analysis of heat build-up curves requires additional inputs from mechanical modelling and from damage investigations.

Acknowledgements

The authors would like to thank the French ANRT agency for its financial support (CIFRE n°2019/1888). This study belongs to the "Self-Heating" ANR - Safran - Naval Group research chair (Grant # ANR-20-CHIN-0002) involving Safran Companies, Naval Group, ENSTA Bretagne (IRDL) and Institut Pprime.

References

1 Leveuf L., Navrátil L., Le Saux V., Marco Y., Olhagaray J. *et al.* Constitutive equations for the cyclic behaviour of short carbon fibre-reinforced thermoplastics and identification on a uniaxial database. *Contin. Mech. Thermodyn.* 2020, 32.2: 403-420.

2 Amjadi M. and Fatemi A. Multiaxial fatigue behavior of thermoplastics including mean stress and notch effects: Experiments and modeling. *Int. J. Fatigue*. 2020, 136: 105571.

3 Santharam P., Marco Y., Le Saux V., Le Saux M., Robert G. *et al.* Fatigue criteria for short fiber-reinforced thermoplastic validated over various fiber orientations, load ratios and environmental conditions. *Int. J. Fatigue*. 2020, 135: 105574.

4 Leveuf L., Marco Y., Le Saux V., Navrátil L., Leclercq S. *et al.*. Fast screening of the fatigue properties of thermoplastics reinforced with short carbon fibers based on thermal measurements. *Polym. Test.* 2018, 68: 19-26.

5 Klimkeit B. *et al.* Multiaxial fatigue life assessment for reinforced polymers. *Int. J. Fatigue*. 2011, vol. 33.6: 766-780.

6 Launay A., Maitournam M. H., Marco Y., and Raoult I. Multiaxial fatigue models for short glass fiber reinforced polyamide – Part I: Nonlinear anisotropic constitutive behavior for cyclic response. *Int. J. Fatigue*. 2013, 47: 382-389.

7 Kawai M., Takeuchi H., Taketa I., and Tsuchiya A. Effects of temperature and stress ratio on fatigue life of injection molded short carbon fiber-reinforced polyamide composite. *Compos. Part Appl. Sci. Manuf.* 2017, 98: 9-24.

8 Malzahn J.C. and Schultz J. M. Tension-tension and compression-compression fatigue behavior of an injection-molded short-glass-fiber/poly(ethylene terephthalate) composite. *Compos. Sci. Technol.* 1986, 27. 4: 253-289.

9 ASTM D575. Standard test method for rubber properties in compression. 2018.

10 Zuo H., Li D., and Jiang L. Experimental study on compressive fatigue behavior and failure mechanism of 3D five-directional braided composites. *Compos. Part Appl. Sci. Manuf.* 2020, 139: 106097.

11 ASTM D6641. Standard test method for compressive properties of polymer matrix composite materials using a combined loading compression (CLC) test fixture. 2021.

12 ASTM D3410. Standard test method for compressive properties of polymer matrix composite materials with unsupported gage section by shear loading. 2021.

13 Horst J. J. and Spoormaker J. L. Mechanisms of fatigue in short glass fiber reinforced polyamide 6. *Polym. Eng. Sci.* 1996, 36.22: 2718-2726.

14 Mandell J. F., Huang D. D., and McGarry F. J. Fatigue of glass and carbon fiber reinforced engineering thermoplastics. *Polym. Compos.* 1981, 2.3: 137-144.

15 Mallick P. K. and Zhou Y. Effect of mean stress on the stress-controlled fatigue of a short E-glass fiber reinforced polyamide-6.6. *Int. J. Fatigue*. 2004, 26.9: 941-946.

16 Mortazavian S. and Fatemi A. Effects of mean stress and stress concentration on fatigue behavior of short fiber reinforced polymer composites. *Fatigue Fract. Eng. Mater. Struct.* 2016, 39.2: 149-166.

17 Bernasconi A., Davoli P., Basile A., and Filippi A. Effect of fibre orientation on the fatigue behaviour of a short glass fibre reinforced polyamide-6. *Int. J. Fatigue*. 2007, 29.2: 199-208.

18 Canegrati A., Martulli L. M., Hine P. J., Grassini C., and Bernasconi A. On the use of milled shell-only specimens to study the effect of fiber orientation on the fatigue behavior of a short fiber-reinforced polyamide. *Fatigue Fract. Eng. Mater. Struct*, 2022

19 Eftekhari M. and Fatemi A. Tensile, creep and fatigue behaviours of short fibre reinforced polymer composites at elevated temperatures: a literature survey. *Fatigue Fract. Eng. Mater. Struct.* 2015, 38.12: 1395-1418.

20 Selzer R. and Friedrich K. Mechanical properties and failure behaviour of carbon fibre-reinforced polymer composites under the influence of moisture. *Compos. Part Appl. Sci. Manuf.* 1997, 28.6: 595-604.

21 Solvay Specialty Polymers. KetaSpire PEEK Design and Processing Guide. *Report.* 2016.

22 Kanters M. J. W., Douven L. F. A., and Savoyat P. Fatigue life prediction of injection moulded short glass fiber reinforced plastics. *Procedia Struct. Integr.* 2019, 19: 698-710.

23 Berrehili A., Castagnet S., and Nadot Y. Multiaxial fatigue criterion for a high-density polyethylene thermoplastic. *Fatigue Fract. Eng. Mater. Struct.* 2010, 33.6: 345-357.

24 Rosa G. L. and Risitano A. Thermographic methodology for rapid determination of the fatigue limit of materials and mechanical components. *Int. J. Fatigue*. 2000, 22.1: 65-73.

25 Doudard C.; Calloch S., Hild F., Cugy P., and Galtier A. Identification of the scatter in high cycle fatigue from temperature measurements. *Comptes Rendus Mécanique*. 2004, 332.10: 795-801.

26 Marco Y., Huneau B., Masquelier I., Le Saux V., and Charrier P. Prediction of fatigue properties of natural rubber based on the descriptions of the cracks population and of the dissipated energy. *Polym. Test.* 2017, 59: 67-74.

27 Meneghetti G. and Quaresimin M. Fatigue strength assessment of a short fiber composite based on the specific heat dissipation. *Compos. Part B Eng.* 2011, 42. 2: 217-225.

28 Chrysochoos A. and Louche H. An infrared image processing to analyse the calorific effects accompanying strain localisation. *Int. J. Eng. Sci.* 2000, 38.16: 1759-1788.

29 Navrátil L., Le Saux V., Leclercq S., Carrere N., and Marco Y. Infrared Image Processing to Guide the Identification of Damage and Dissipative Mechanisms in 3D Layer-to-Layer Woven Composites. *Appl. Compos. Mater.* 2022, 29.4: 1449-1477.

30 Le Saux V. Celenos user manual. *Internal report*. ENSTA Bretagne. IRDL. 2022.

31 Breitenstein O., Warta W. and Langenkamp M. Lock-in thermography: Basics and use for evaluating electronic devices and materials. Berlin: Springer. 2010.

32 Navrátil L., Leveuf L., Le Saux V., Marco Y., Olhagaray J. *et al.* A model to describe the cyclic anisotropic mechanical behavior of short fiber-reinforced thermoplastics. *Mech. Time-Depend. Mater.* 2020, 24.4: 481-503